

Received 5 May 2023, accepted 15 May 2023, date of publication 23 May 2023, date of current version 1 June 2023.

Digital Object Identifier 10.1109/ACCESS.2023.3279107

## RESEARCH ARTICLE

# A Flexible Rooftop Photovoltaic-Inductive Wireless Power Transfer System for Low-Voltage DC Grid

IO-WA IAM<sup>1,2,3</sup>, (Student Member, IEEE), ZHAOYI DING<sup>1,2,3</sup>, (Student Member, IEEE), ZHICONG HUANG<sup>1,2,3,4</sup>, (Member, IEEE), CHI-SENG LAM<sup>1,2,3</sup>, (Senior Member, IEEE), RUI P. MARTINS<sup>1,2,3,5</sup>, (Fellow, IEEE), AND PUI-IN MAK<sup>1,2,3</sup>, (Fellow, IEEE)

<sup>1</sup>State Key Laboratory of Analog and Mixed-Signal VLSI, University of Macau, Macao, China

<sup>2</sup>Institute of Microelectronics, University of Macau, Macao, China

<sup>3</sup>Department of Electrical and Computer Engineering, Faculty of Science and Technology, University of Macau, Macao, China

<sup>4</sup>Shien-Ming Wu School of Intelligent Engineering, South China University of Technology, Guangzhou 510006, China

<sup>5</sup>Instituto Superior Técnico, Universidade de Lisboa, 1049-001 Lisbon, Portugal

Corresponding author: Chi-Seng Lam (cslam@um.edu.mo; c.s.lam@ieee.org)

This work was supported in part by the Science and Technology Development Fund, Macau SAR (FDCT), under Grant 0014/2021/ITP, Grant 0028/2020/A1, Grant 0027/2021/A1, Grant SKL-AMSV(UM)-2020-2022, and Grant SKL-AMSV(UM)-2023-2025; and in part by the Shenzhen Science and Technology Innovation Commission (SZSTI) under Grant SGDX20201103093601011.


**ABSTRACT** A rooftop photovoltaic (PV) system is a significant solution of building-integrated centralized generation in the low-voltage (LV) DC grid. The drilling-free rooftop PV-inductive wireless power transfer (PV-IWPT) system for the LVDC grid can reduce the installation and post-maintenance costs, with the elimination of physical cable connections and preventing breaking of thermal bridge and rain penetration between the rooftop and the inside of the building. Moreover, it has inherent isolation properties between the input and the output terminals. However, it is challenging for the PV-IWPT system to simultaneously achieve the maximum power point tracking (MPPT) for the PV panels and the maximum efficiency point tracking (MEPT) for the system even under diverse irradiance conditions. In this paper, we propose an efficient PV-IWPT system, which consists of a series-series IWPT converter, driven by the PV panels and loaded by the LVDC grid directly. Moreover, we apply in the proposed system a particle swarm optimization with an auxiliary Perturb and Observe (P&O) algorithm and a load matching method without wireless feedback communication to realize MPPT and MEPT in the overall PV-IWPT system simultaneously. Finally, we analyze theoretically and verify experimentally the proposed PV-IWPT system in a 500-W experimental platform under different irradiance conditions.

**INDEX TERMS** Low-voltage DC grid, photovoltaic, maximum power point tracking, inductive wireless power transfer, maximum efficiency point tracking.

## NOMENCLATURE

|         |   |
|---------|---|
| RESs    | Renewable energy sources.                       |
| LVDC    | Low voltage dc.                                 |
| PV      | Photovoltaic.                                   |
| PV-IWPT | Photovoltaic-inductive wireless power transfer. |
| MPPT    | Maximum power point tracking.                   |

|         |  |
|---------|--|
| MEPT    | Maximum efficiency point tracking.               |
| P&O     | Perturb and observe algorithm.                   |
| SS-IWPT | Series-series inductive wireless power transfer. |
| SAR     | Semi-active rectifier.                           |
| PSO     | Particle swarm optimization.                     |
| MPP     | Maximum power point.                             |
| PWM     | Pulse width modulation.                          |
| ZPA     | Zero phase angle.                                |
| FHA     | Fundamental harmonic analysis.                   |
| KVL     | Kirchhoff's voltage law.                         |
| GMPP    | Global maximum power point.                      |

The associate editor coordinating the review of this manuscript and approving it for publication was Ahmed F. Zobaa .

This work is licensed under a Creative Commons Attribution-NonCommercial-NoDerivatives 4.0 License.  
For more information, see <https://creativecommons.org/licenses/by-nc-nd/4.0/>

|                           |  |  |   |
|---------------------------|--|--|---|
| $L_P, L_S$                | Self-inductances of the transmitter and the receiver sides.              | $v_{P,avg}, i_{P,avg}$   | Average value of $v_p$ and $i_p$ .  |
| $M$                       | Mutual inductance.   | $R_{on,1}, R_{on,2}$   | On-resistance of the MOSFET switches.   |
| $k$                       | Coupling coefficient.  | $V_{f,1}, V_{f,2}$   | Forward voltage of the anti-parallel diode of the switch in the inverter and the SAR.                   |
| $R_{P,w}, R_{S,w}$        | Coil losses at the transmitter and the receiver sides.                   | $i_{P,rms}, i_{S,rms}$   | Rms value of $i_p$ and $i_s$ .  |
| $C_P, C_S$                | Series compensation capacitors at the transmitter and receiver sides.    | $P_{sw,SAR}, P_{con,SAR}$  | Switching loss and conduction loss of the SAR.  |
| $\omega_P, \omega_S$      | Resonant angular frequencies at the transmitter and receiver sides.      | $P_{loss,SAR}$   | Power loss of the SAR.  |
| $V_{IN}, I_{IN}$          | dc input voltage and current extracted from the PV array.                | $v_{S,avg}, i_{S,avg}$   | Average value of $v_s$ and $i_s$ .  |
| $v_P, v_S$                | ac voltage at the transmitter and receiver sides.                        | $R_P, R_S$   | Equivalent series resistance of the transmitter side and receiver side.                                 |
| $i_S$                     | ac current for the SAR.  | $p_{Best}, G_{Best}$   | Local best position of a particle in a searching area and global best position of the whole population. |
| $C_{f,p}, C_{f,s}$        | Input and output capacitor.  | $i$  | Particle size.  |
| $V_O, I_O$                | dc output voltage and current of the PV-IWPT converter.                  | $v_i, x_i$   | Velocity and position of each particle.   |
| $S_1 - S_4$               | Four sic MOSFET switches in the inverter.                                | $t$  | $t$ -th iteration.  |
| $S_7, S_8$                | Two MOSFET switches at the lower legs of the SAR.                        | $p$  | Fitness function of PSO.  |
| $D_5, D_6$                | Two diodes at the upper legs of the SAR.                                 | $r_{out,Tx}, r_{out,Rx},$<br>$r_{in,Tx}, r_{in,Rx},$<br>$N_{Tx}, N_{Rx}$ | Outer radius, inner radius, number of turns of the transmitter-side and the receiver-side Coils.        |
| $\alpha, \beta$           | The conduction angle of $v_p$ and $v_s$ .                                |  |   |
| $v_{P,1}, v_{S,1}$        | The fundamental components of $v_p$ and $v_s$ .                          |  |   |
| $R_{LVDC}$                | Load resistor.   |  |   |
| $V_P, I_P, V_S$ and $I_S$ | The phasors of the fundamental components of $v_p, i_p, v_s$ and $i_s$ . |  |   |
| $R_{eq}$                  | Equivalent resistance of the SAR with $R_{LVDC}$ .                       |  |   |
| $X_M$                     | The impedance of mutual inductance.                                      |  |   |
| $Z_P, Z_S$                | The impedance at the transmitter-side and the receiver-side.             |  |   |
| $\omega_{opt}$            | Optimum operating frequency.   |  |   |
| $R_{eq,opt}$              | Optimum load resistance.   |  |   |
| $P_{OUT}$                 | Output power of the PV-IWPT converter.                                   |  |   |
| $P_{MAX}$                 | Maximum power extracted from PV panel.                                   |  |   |
| $R_{IN,MAX}$              | Maximum power dc input resistance value.                                 |  |   |
| $R_{IN}$                  | The dc input resistance of the PV-IWPT converter.                        |  |   |
| $Z_{ref}$                 | Equivalent impedance reflected from the receiver-side.                   |  |   |
| $Z_{in}$                  | Input impedance of the PV-IWPT converter.                                |  |   |
| $P_{loss,inv}$            | Power loss of the inverter.  |  |   |
| $P_{sw,inv}, P_{con,inv}$ | Switching loss and conduction loss of the inverter.                      |  |   |
| $t_{on}, t_{off}$         | Turn-on time and turn-off time of the MOSFET switches.                   |  |   |
| $C_{oss,1}, C_{oss,2}$    | Output capacitance of each MOSFET switch in the inverter and the SAR.    |  |   |

I. INTRODUCTION

Nowadays, due to the rapid growth of the energy demand, the reliance on the renewable energy sources (RESs) increases progressively in the distribution power systems, as well as relieving severe environmental pollutions [1], [2]. Therefore, RESs play a significant role in complementing the high-energy-density but environmental-friendless non-renewable energy sources. Clean electricity can come from the distributed RESs, including photovoltaic energy, wind energy, biogas energy, etc. Among the aforementioned RESs, the improvement of PV technology distinguishes itself leading to its wide utilization due to the abundance of solar irradiation [3], [4]. Meanwhile, since the majority of the electronic devices exclusively operate on DC power and a number of distributed RESs produce energy in DC, the recent wide-application of a low voltage DC (LVDC) grid allows the interconnection of the main power bus with the loads and the various energy sources [5], [6], [7], [8]. Furthermore, the LVDC grid is a promising way to materialize and overcome the limitations of the AC power grid, by enhancing the conversion efficiency through cost reduction and avoiding the inherent synchronization and stability problems [5], [9]. Fig. 1 presents an example of local energy exchange, composed by interconnect generation, energy storage and load consumption. However, the centralized RES generation plays an important role for the LVDC grid and paves the way for the sustainable improvement of LVDC grid. The rooftop PV system (Fig. 2(b)) is a significant development solution of the building-integrated centralized generation in the LVDC grid, installed in

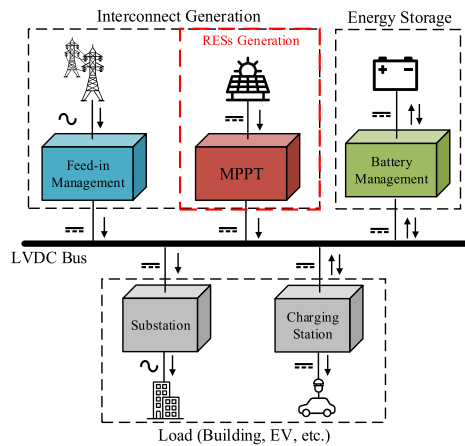


FIGURE 1. Schematic overview of a typical low-voltage DC grid.

modern timber-roofs [10], [11]. Compared with the conventional rooftop PV modules (Fig.2(a)) that usually require fixed cable-connections among the PV array, the power converters and the building's loads, the obvious merits of the proposed PV-IWPT system omit the complicated wiring design of the wall and simplify the installation steps by getting rid of the physical cable connections between the rooftop and the building inside, which are mainly provided by IWPT technique [12], [13], [14]. Especially, a study in [15] has shown that solving the wiring issues of rooftop PV can effectively shorten the installation time within one day and also reduce the labor cost by 30-40%, which is a significant cost driven for the rooftop PV installation. Thus, the installation cost of the proposed PV-IWPT system can be reduced including the reduction of time cost, labor cost and construction cost. Moreover, the drilling-free PV-IWPT system avoids the thermal discomfort caused by breaking the thermal bridge of buildings and the rain penetration that damages the interior of the buildings and then destroy the overall function of the PV system, so it can also lower the post-maintenance cost [16], [17]. Furthermore, the wiring connection issue will also affect the system's overall performance. After installation, a wiring issue will also result in significant maintenance issues [18]. Fig. 2(c) shows the cross-section view of the proposed rooftop PV-IWPT system. Since it is convenient to install and remove, the rooftop PV-IWPT system has a great potential for application. More importantly, the PV-IWPT system has inherent isolation properties between the input and the output terminal by making use of the loosely-coupler (Transmitter and receiver coils) as same as the widely used isolated DC-DC converter using a transformer for conventional wired PV system [19].

Due to the non-linear relationship between the output current and the voltage of the PV array and the rather complex relationship between the input and output characteristics of the IWPT converter, it is a challenge to maintain both the maximum power point tracking (MPPT) and the maximum efficiency point tracking (MEPT) simultaneously for the

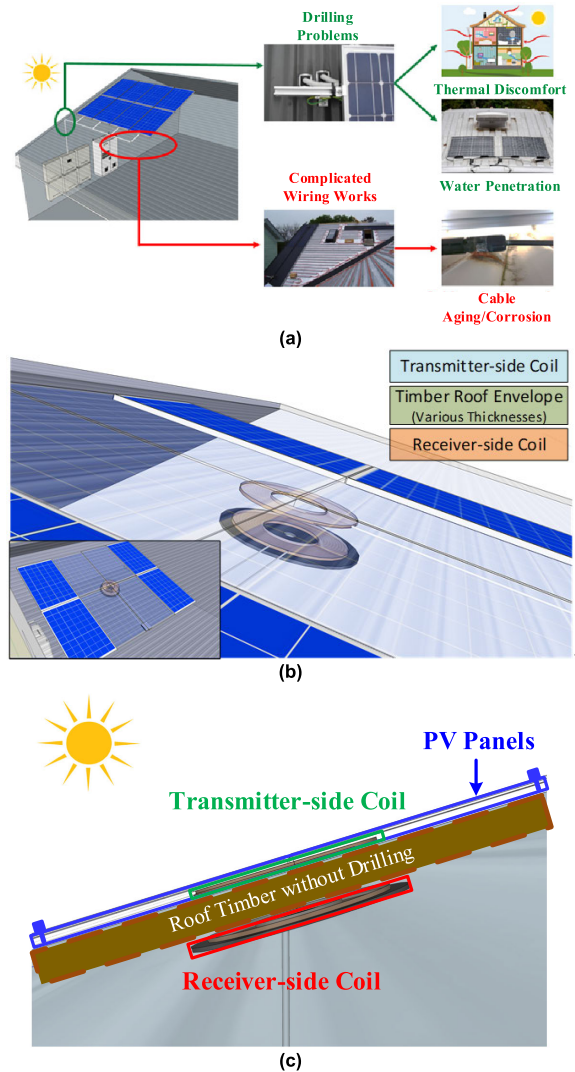


FIGURE 2. Construction overview of timber-rooftop PV system: (a) Conventional rooftop PV system; (b) Proposed rooftop PV-IWPT system; (c) The cross-section view of proposed PV-IWPT system.

overall PV-IWPT system. In terms of the implementation of the MPPT operation, some PV systems integrated with the IWPT converter has proposed and emerged recently [20], [21], [22], [23], [24], in which an additional DC-DC converter was applied between the PV array and the inverter of the IWPT converter to implement the MPPT control algorithm, thus increasing the cost. Additionally, keeping the characteristic of the PV array under various irradiation conditions including non-shading condition, uniform shading condition and partial shading condition, the pure PV system usually requires the adoption of various maximum power tracking algorithms [25], [26], [27], which targets for the minimization of the cost and the maximization of the conversion efficiency of the PV array. Unfortunately, most of the PV-IWPT systems in the existing literature [20], [21], [22], [23], [24], [28], [29] did not consider the shading issues. The wireless power

transfer system interfacing with a DC bus in [29] did not take into account the shading conditions as well.

Shading issues significantly influence the output power of the PV-IWPT system, resulting in a wide equivalent load variation for the IWPT converter. Besides, load impedance mismatch also causes a significant transfer efficiency degradation for the IWPT converter [30], [31], [32], [33]. Unfortunately, all of the aforementioned PV-IWPT systems did not consider load impedance matching in their designs, thus the transfer efficiency is not optimized in [20], [21], [22], [23], [24], [28], and [29]. Since the load variation under shading conditions is normally wide, it is challenging to maintain the operation of the MEPT by using a single-stage IWPT.

To fill up the gap of the PV-IWPT system, this work presents and explores a single-stage series-series IWPT (SS-IWPT) converter directly driven by a PV array and adopted a full bridge inverter at the transmitter-side and semi-active rectifier (SAR) at the receiver-side (Fig. 3). The input resistance of the IWPT converter determines the output power of the PV array. The inverter at the transmitter-side is responsible for the implementation of the PV's MPPT under a constant operation frequency. To verify the feasibility of the proposed system under various irradiance conditions and even rainy issue, we adopt a particle swarm optimization (PSO) with auxiliary Perturb and Observe (P&O) hybrid algorithm in the proposed PV-IWPT system to realize global maximum power point (MPP) of the PV array. Moreover, the SAR at the receiver-side is solely responsible for maintaining the maximum transfer efficiency via the phase-shift pulse width modulation (PWM), thus wireless feedback communication between the transmitter and receiver sides is not required. In addition, the transfer distance conforms to the actual thickness of rooftop timber. In this paper, the properties and contributions of the proposed PV-IWPT system are summarized in the following:

- Drilling-free and less wiring works, resulting in lower installation cost;
- Avoid of the thermal discomfort and water penetration, resulting in lower maintenance cost;
- High overall efficiency by achieving MPPT of the PV array and MEPT of the whole PV-IWPT converter system simultaneously, which are lack of consideration for the existing PV-IWPT systems;
- Well operating in various shading conditions and even under rainy issue, which is lack of consideration for the existing PV-IWPT systems;
- A single-stage SS-IWPT converter saves the size and cost of the whole system, and has inherent isolation properties;
- Eliminate the feedback wireless communication requirement with the PV-IWPT operating at a fixed frequency.

The comparison of the conventional PV-IWPT systems and this work are summarized in Table 1. The remaining of paper has the following organization. Section II describes the proposed PV-IWPT system, including its structure, operational

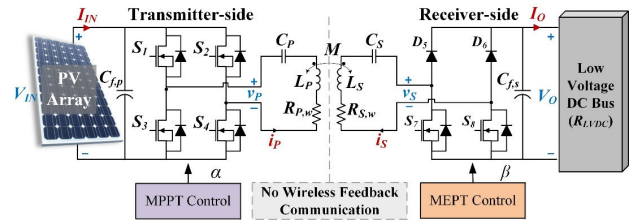


FIGURE 3. Circuit configuration of the proposed PV-IWPT system and its control scheme.

waveforms of the inverter and the SAR, equivalent circuit analysis, and considerations about different irradiance conditions. Then, we will analyze and discuss the efficiency and the operation of the MEPT and the MPPT via the equivalent circuit model proposed in Section III. In Section IV, we present the implementation of the proposed control scheme for the PV-IWPT system, with the experimental verification presented in Section V. Finally, Section VI draws the conclusions of this paper.

## II. PROPOSED PV-IWPT SYSTEM

### A. TEMPLATE SYSTEM STRUCTURE

Fig. 3 exhibits the proposed PV-IWPT system, where the PV array at the transmitter-side drives the SS-IWPT, with the SAR implemented for direct efficiency optimization at the receiver-side. In the schematics of the PV-IWPT converter, the magnetic coupler has self-inductances  $L_p$  and  $L_s$ , and mutual inductance  $M$ . We can define the coupling coefficient for this PV-IWPT system as  $k = \frac{M}{\sqrt{L_p L_s}}$ . The resistances  $R_{p,w}$  and  $R_{s,w}$  represent the coil losses at the transmitter and the receiver sides, respectively, while  $C_p$  and  $C_s$  are the series compensation capacitors at the transmitter and receiver sides, respectively, with the resonant angular frequencies  $\omega_p = \frac{1}{\sqrt{L_p C_p}}$  and  $\omega_s = \frac{1}{\sqrt{L_s C_s}}$  [34], [35].  $V_{IN}$  and  $I_{IN}$  are the dc input voltage and current extracted from the PV array. The PV array act as a voltage source modulated into ac voltage  $v_p$  in a constant angular frequency to drive the resonant circuit at the transmitter-side, by using a full-bridge inverter that consists of four SiC MOSFET switches  $S_1 - S_4$ . And a high-capacitance input capacitor  $C_{f,p}$  is required to minimize the current pulsation in the PV panels [36]. At the receiver-side, the ac voltage  $v_s$  and ac current  $i_s$  are the inputs for the SAR which consists of two diodes  $D_5$  and  $D_6$  at the upper legs, and two MOSFET switches  $S_7$  and  $S_8$  at the lower legs. The SAR is parallel connected with a large output capacitor,  $C_{f,s}$ .  $V_O$  and  $I_O$  are the dc output voltage and current of the PV-IWPT converter, respectively. Since the output of the PV-IWPT system connects to the LVDC bus,  $V_O$  should be the same as the voltage of the LVDC bus.

### B. OPERATIONAL WAVEFORMS OF INVERTER AND SAR

Fig. 4 shows the operational waveforms of the inverter and the SAR, in which the switches of the inverter  $S_1-S_4$  and the semi-active rectifier  $S_7-S_8$  turn on and off in an appropriate

TABLE 1. Comparison of the conventional PV-IWPT systems and this work.

| Different works                                 | [20]                 | [21]                 | [22]                 | [23]            | [24]            | [28]            | [29]           | This work  |
|---|----------------------|----------------------|----------------------|-----------------|-----------------|-----------------|----------------|--|
| Complexity of Compensation Topology             | High (LCL-S)         | High (LCL-S)         | Low (S-S)            | Low (S-S)       | Low (S-S)       | High (L2CL-LCL) | Low (S-S)      | Low (S-S)  |
| Without Additional DC-DC Converter              | No (No.:1)           | No (No.:1)           | No (No.:1)           | No (No.:1)      | No (No.:1)      | Yes             | Yes            | Yes  |
| Constant Operating Frequency                    | Yes                  | Yes                  | No                   | Yes             | No              | Yes             | No             | Yes  |
| Transfer Distance                               | NA (Simulation Only) | NA (Simulation Only) | NA (Simulation Only) | 100mm (Gap:Air) | 100mm (Gap:Air) | NA              | 75mm (Gap:Air) | 140mm (Gap: Timber)                                      |
| Consideration of MEPT (Load Impedance Matching) | No                   | No                   | No                   | No              | No              | No              | No             | Yes  |
| Consideration of Various Shading Condition      | No                   | No                   | No                   | No              | No              | No              | No             | Yes (Both uniform shading and partial shading condition) |
| No Wireless Feedback Communication              | Yes                  | Yes                  | No                   | Yes             | Yes             | Yes             | Yes            | Yes  |
| Consideration of Rainy Issues                   | No                   | No                   | No                   | No              | No              | No              | No             | Yes  |

Note: The shaded areas mean the desirable performance.

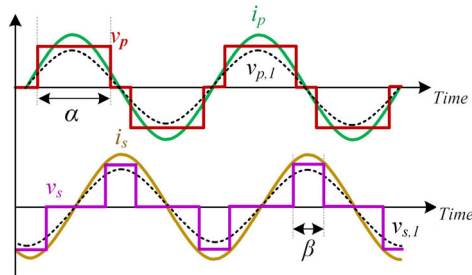


FIGURE 4. The operational waveforms of the inverter (Upper part) and the SAR (Lower part).

driving sequence to generate the corresponding waveforms. The upper part illustrates the operational waveforms of the inverter, aiming to adjust the input resistance of the PV-IWPT converter by modifying the conduction angle  $\alpha$  of  $v_p$ , and  $v_{p,1}$  is the fundamental component of  $v_p$ , always kept aligned with the  $i_p$ . Similarly, the lower part illustrates the operational waveforms of the SAR, aiming to adjust the conduction angle  $\beta$  by  $v_s$  to match the optimum load, and  $v_{s,1}$  is the fundamental component of  $v_s$  that kept aligned with  $i_s$ . Since the fundamental components of  $v_p$  and  $v_s$  are in phase with  $i_p$  and  $i_s$ , respectively, the characteristic of zero phase angle (ZPA) can minimize the converter voltage-ampere rating by eliminating the reactive power caused by the modulation.

Since the resonant circuit output voltage and current ( $v_s$  and  $i_s$ ) to the SAR are in phase, it is acceptable to model the load as a resistor. Moreover, assuming that the PV-IWPT system is well-decoupled with the LVDC bus through a large decoupling capacitor  $C_{f,s}$  [19] and the proposed PV-IWPT system operates at a fixed frequency, we can model the LVDC bus as a load resistor,  $R_{LVDC}$  [37].

### C. EQUIVALENT CIRCUIT ANALYSIS

Fig. 5 presents the equivalent circuit model of the SS-IWPT converter, based on the fundamental harmonic analysis

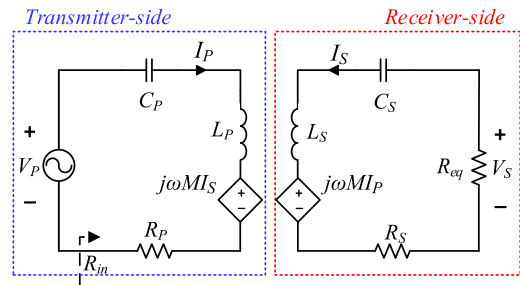


FIGURE 5. AC equivalent circuit model of the SS-IWPT.

(FHA). Since the SS-IWPT converter operates at the resonant frequency and is a high-quality-factor circuit, this model is sufficiently accurate for the subsequent analysis [38], [39], [40]. Here, we divide the equivalent circuit model into the transmitter loop and the receiver loop.  $V_p$ ,  $I_p$ ,  $V_s$  and  $I_s$  are the phasors of the fundamental components of  $v_p$ ,  $i_p$ ,  $v_s$  and  $i_s$ , respectively. The series resistance  $R_p$  includes the coil loss  $R_{p,w}$  and the loss from the inverter at the transmitter-side, while the series resistance  $R_s$  includes the coil loss  $R_{s,w}$  and the loss from the SAR at the receiver-side. According to Kirchhoff's voltage law (KVL), we can deduce the basic equations for the circuit model as:

$$[R_p + j(\omega L_p - \frac{1}{\omega C_p})]I_p - j\omega M I_s = V_p \quad (1)$$

$$-[R_s + R_{eq} + j(\omega L_s - \frac{1}{\omega C_s})]I_s + j\omega M I_p = 0 \quad (2)$$

Moreover, we can represent the SAR together with the LVDC bus load  $R_{LVDC}$  by an equivalent resistance  $R_{eq}$ :

$$R_{eq} = \frac{8}{\pi^2} R_{LVDC} \sin^2(\frac{\beta}{2}) \quad (3)$$

Therefore, from (1)-(2), the equation of  $I_s$  is:

$$I_s = \frac{jX_M}{Z_S Z_P + X_M^2} V_p \quad (4)$$

where  $X_M = \omega M$ ,  $Z_p = j\omega L_p + \frac{1}{j\omega C_p} + R_p$  and  $Z_S = j\omega L_S + \frac{1}{j\omega C_S} + R_S + R_{eq}$  are the impedance at the transmitter-side and the receiver-side, respectively.

The magnitudes of  $V_p$  and  $I_p$  are:

$$|V_p| = \frac{4}{\pi} V_{IN} \sin\left(\frac{\alpha}{2}\right) \tag{5}$$

$$|I_p| = \frac{\pi}{2} \frac{I_{IN}}{\sin\left(\frac{\alpha}{2}\right)} \tag{6}$$

**D. CASES OF VARIOUS SHADING CONDITIONS**

The different shading conditions cause the PV array to exhibit inconsistent MPP for the SS-IWPT converter. However, the equivalent load of the LVDC bus is:

$$R_{LVDC} = \frac{V_O^2}{P_{OUT}} \tag{7}$$

The solar irradiance directly influences the output power of the PV-IWPT converter, resulting in a wide load range variation for the PV-IWPT converter. Hence, this situation for the proposed PV-IWPT system becomes more complex with the PV array subjected to the variation of irradiance conditions.

In this paper, Fig. 6 shows six different cases of PV array operating under different shading conditions for the proposed PV-IWPT system. The PV array consists of four strings of two series-connected 1STH-215-P modules supplied by Soltech, and we emulate a total of 6 different irradiance cases with this testing PV array. Fig. 7 (a)-(d) plot the P-V and I-V characteristics curves of this PV array from Case 1 to Case 6, respectively and highlight their corresponding key specifications. Moreover, we can sub-divide these six cases into three general conditions where Case 1 represents non-shading condition, Case 2-Case 4 represent uniform shading conditions, and Case 5-Case 6 represent partial shading conditions. Since this paper only considers the influence of different solar irradiations, we keep the same temperature at 25°C for all the cases.

**III. ANALYSIS OF MEPT AND MPPT OPERATION**

**A. OPERATION OF THE MEPT AT THE SAR**

From Fig. 5, the transfer efficiency is [41]:

$$\begin{aligned} \eta &= \frac{|I_S|^2 R_{eq}}{|I_S|^2 R_{eq} + |I_S|^2 R_S + |I_p|^2 R_p} \\ &= \frac{X_M^2 R_{eq}}{[(R_{eq} + R_S)^2 + X_S^2] R_p + (R_S + R_{eq}) X_M^2} \end{aligned} \tag{8}$$

To achieve the maximum power transfer efficiency, the optimum operating frequency  $\omega_{opt}$ , and the optimum load resistance  $R_{eq,opt}$  [42], are:

$$\omega_{opt} = \omega_S \tag{9}$$

$$R_{eq,opt} = X_M \sqrt{\frac{R_S}{R_p}} \tag{10}$$

**TABLE 2. Simulation parameters.**

| Symbol                 | Parameter                | Value              |
|------------------------|--------------------------|--------------------|
| $L_p, L_S$             | Self-inductance          | 255.50μH, 375.40μH |
| $k$                    | Coupling coefficient     | 0.235              |
| $R_p, R_S, R_{sw}$     | Coil resistance          | 0.25Ω, 0.50Ω       |
| $f_{sw} = \omega/2\pi$ | Operating frequency      | 50kHz              |
| $C_p, C_S$             | Compensation capacitance | 39.65nF, 29.99nF   |
| $R_{eq,opt}$           | Optimum load resistance  | Fixed at 32Ω       |

As discussed in Section II-D, the equivalent load of the LVDC bus  $R_{LVDC}$  is varying according to the output power of the PV-IWPT converter, which is assumed to be the same as the input power extracted from the PV array. From Fig. 8, the  $R_{LVDC}$  becomes larger, while the  $P_{OUT}$  is smaller when the solar irradiance is low, and vice versa. This results in a wide load range  $R_{LVDC}$  variation, and a wide  $R_{eq}$  variation in the PV-IWPT converter, which is due to the variation of the irradiance, thus degrading the transfer efficiency a lot. In order to keep the equivalent resistance  $R_{eq}$  to its optimum value  $R_{eq,opt}$  for the PV-IWPT converter, we should adjust the conduction angle  $\beta$  of the SAR according to different irradiance conditions. Hence, combining (3) and (10), we can obtain:

$$R_{eq,opt} = R_{eq} = \frac{8}{\pi^2} R_{LVDC} \sin^2\left(\frac{\beta}{2}\right) \tag{11}$$

From (11), we can derive the conduction angle  $\beta$  as:

$$\beta = 2 \arcsin \sqrt{\frac{X_M \sqrt{\frac{R_S}{R_p}}}{\frac{8}{\pi^2} \frac{V_O^2}{P_{OUT}}}} \tag{12}$$

From (12), we determine the conduction angle  $\beta$  of the SAR through the output power, output voltage, and the optimum load of the PV-IWPT converter. Based on the simulated parameters as shown in Table 2, Fig. 8 shows the simulation results of the optimum conduction angle  $\beta$  versus the output power  $P_{OUT}$ . When the output power decreases, which also reflects that the solar irradiance decreases, the conduction angle  $\beta$  should decrease accordingly in order to keep the optimum power transfer efficiency, and vice versa.

**B. OPERATION OF THE MPPT AT THE INVERTER**

Typically, the output power of the PV array depends on the DC input resistance of the PV-IWPT converter [43]. Supposing that we can extract the maximum power  $P_{MAX}$  at a maximum power DC input resistance value,  $R_{IN,MAX} = \frac{V_{mpp}^2}{P_{MAX}}$ , where  $V_{mpp}$  is the corresponding voltage of MPP. In order to extract the maximum output power  $P_{MAX}$  from the PV array, the DC input resistance of the PV-IWPT converter  $R_{IN}$  should satisfy:

$$R_{IN} = R_{IN,MAX} \tag{13}$$

Since the DC input resistance of the PV-IWPT converter can be derived as  $R_{IN} = \frac{V_{IN}}{I_{IN}}$ , with the help of (5), (6) and (13),

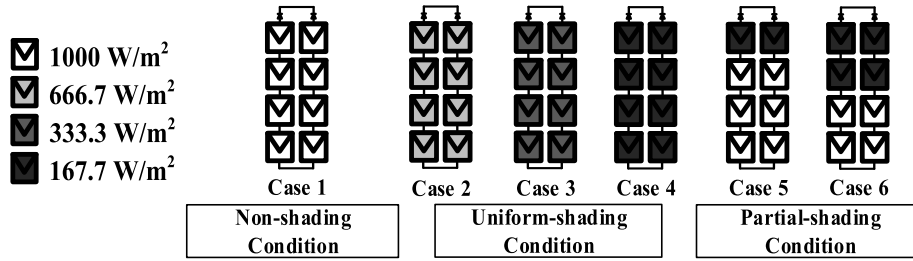


FIGURE 6. Cases of PV array operating under non-shading condition, uniform shading conditions and partial shading conditions.

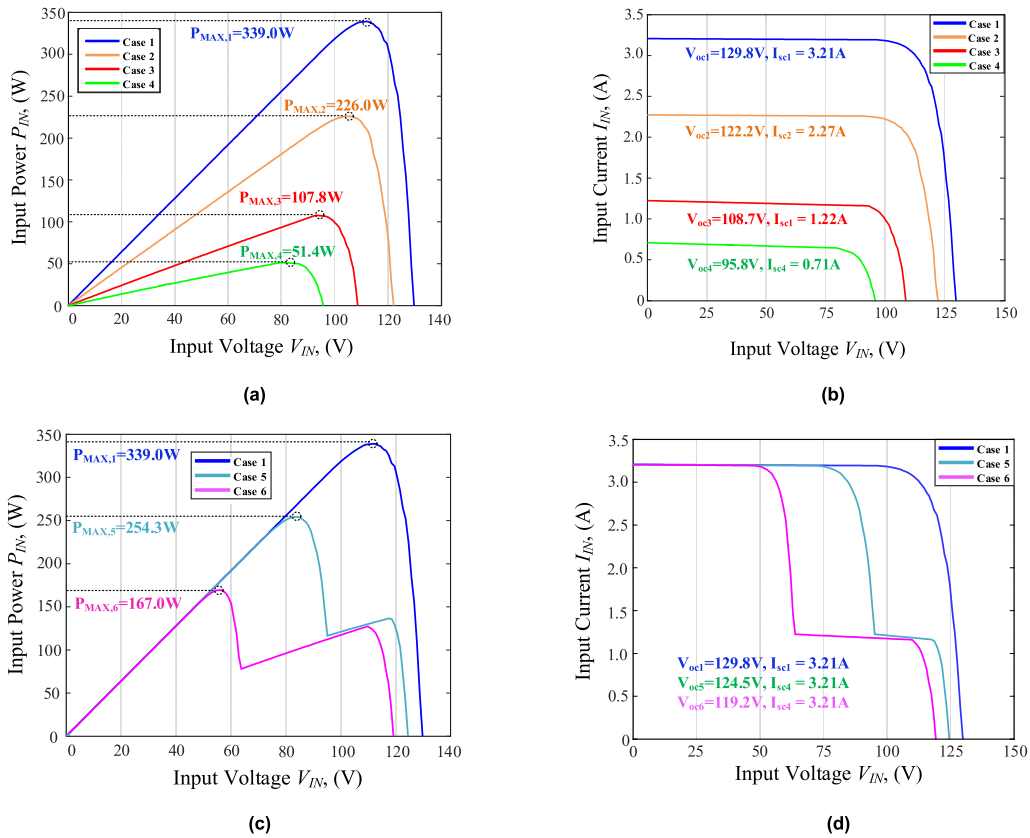


FIGURE 7. Characteristics of the PV array under non-shading shading and uniform shading condition: (a) P-V curves of Case 1-4; (b) I-V curves of the PV array under partial shading condition: (c) P-V curves of Case 1, Case 5 and 6; (d) I-V curves of Case 1, Case 5 and 6.

we can obtain that the conduction angle  $\alpha$  of the inverter should satisfy:

$$R_{IN,MAX} = \frac{R_{in}}{\frac{8}{\pi^2} \sin^2 \frac{\alpha}{2}} \quad (14)$$

provided that the PV-IWPT converter is required to extract the maximum power from the PV panels. Aiming to analyze the ac input resistance  $R_{in}$  of the PV-IWPT converter, we can decouple the transmitter loop from the receiver loop as represented in Fig. 5, in which we can replace the dependent source  $j\omega MI_S$  at the transmitter-side by an equivalent impedance reflected from the receiver-side  $Z_{ref} = \frac{X_M^2}{Z_S + R_{eq}}$ , then we can

analyze the input impedance  $Z_{in}$  as:

$$Z_{in} = Z_P + \frac{X_M^2}{Z_S + R_{eq}} \quad (15)$$

With a unity ratio of  $\frac{\omega P}{\omega S}$  and the operating frequency chosen at  $\omega_{opt}$ , we can compensate well the inductance  $L_P$  and  $L_S$  with the compensation capacitors  $C_P$  and  $C_S$ , respectively. Then, if the SAR tightly operates the MEPT control, we can obtain the ac input resistance  $R_{in}$  as:

$$R_{in} = R_P + \frac{1}{\frac{R_S}{X_M^2} + \frac{1}{X_M} \sqrt{\frac{R_S}{R_P}}} \quad (16)$$

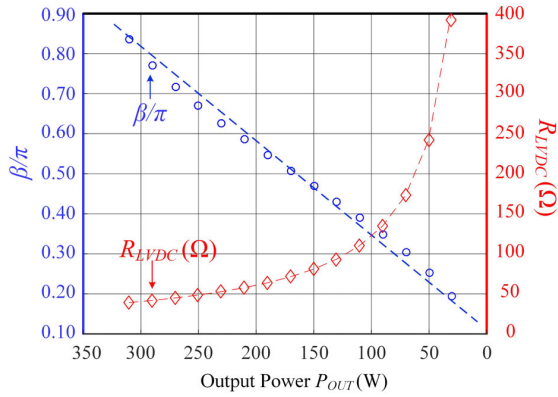


**FIGURE 8.** Cases of PV array operating under non-shading condition, uniform shading conditions and partial shading conditions. Conduction angle  $\beta$  of the SAR, equivalent load of LVDC bus  $R_{LVDC}$  versus output power  $P_{OUT}$ .

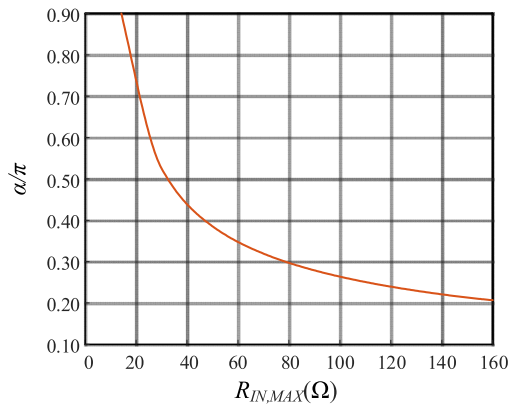


**FIGURE 9.** Conduction angle  $\alpha$  of the inverter versus maximum power DC input resistance  $R_{IN,MAX}$ .

Thus, with the help of (14) and (16), we can derive the conduction angle  $\alpha$  of the inverter as:

$$\alpha = \frac{\pi}{\sqrt{2}} \arcsin \sqrt{\frac{R_P + \frac{1}{\frac{R_S}{X_M^2} + \frac{1}{X_M} \sqrt{\frac{R_S}{R_P}}}}{R_{IN,MAX}}} \quad (17)$$

From (17), we can determine the optimum operation of the conduction angle  $\alpha$  of the inverter by using the  $R_{IN,MAX}$ , which mainly depends on the solar irradiance condition, thus the MPPT is achieved by controlling the inverter with different  $\alpha$ , while the MEPT is achieved by controlling the SAR with different conduction angle  $\beta$  accordingly. Fig. 9 shows the simulation results of the optimum conduction angle  $\alpha$  of the inverter versus different maximum power DC input resistance  $R_{IN,MAX}$  to achieve MPPT.

#### IV. IMPLEMENTATION OF MEPT AND MPPT CONTROL SCHEMES FOR THE PV-IWPT SYSTEM

Based on the operation principles of the MEPT and MPPT for the PV-IWPT system discussed in Section III-A and III-B, respectively, we can independently control the inverter at

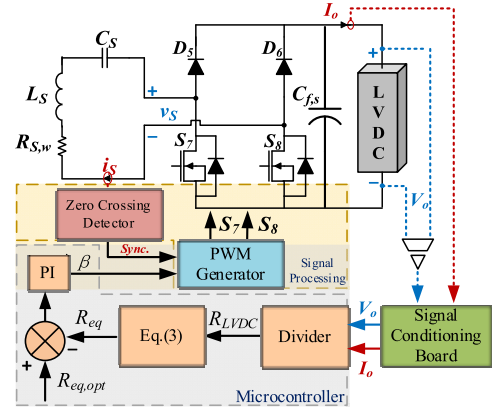


**FIGURE 10.** MEPT control scheme of the proposed PV-IWPT system.

the transmitter-side and the SAR at the receiver-side without requiring a feedback wireless communication between them.

#### A. MEPT CONTROL SCHEME

From (11), we can modulate the equivalent load resistance  $R_{eq}$  for the PV-IWPT converter to the optimum value  $R_{eq,opt}$  by controlling the conduction angle  $\beta$  of the SAR. Fig. 10 exhibits the MEPT control scheme at the receiver side of the proposed PV-IWPT system. First of all, based on the discussion in Section II-D, the variation of the solar irradiance will change the  $R_{LVDC}$  value. A signal conditional board senses the output voltage  $V_O$  and the output current  $I_O$ . Next, we can calculate the  $R_{LVDC}$  by using a divider. After that, we can obtain the value of the equivalent resistance  $R_{eq}$  based on (3). Then, we subtract the calculated  $R_{eq}$  from the reference value of the optimum load resistance  $R_{eq,opt}$  to obtain the equivalent resistance error. Subsequently, a simple PI controller applies the correction to the equivalent resistance error, to form a control signal  $\beta$  for the PWM generation for the SAR. The utilization of a zero-crossing detection of  $i_S$  generates a synchronization signal for the PWM generation. In this way, the PWM generator can drive the SAR to realize the operation of the MEPT. However, the control reference  $R_{eq,opt}$  is significant for this load matching control.

From (10), it is noting that theoretically the optimum load resistance  $R_{eq,opt}$  varies with the variation of losses resistance ratio  $\sqrt{\frac{R_P}{R_S}}$ , with  $X_M$  in (10) being a constant. According to the equivalent circuit analysis in Section II-C,  $R_P$  and  $R_S$  include the power loss from the inverter and the SAR except for each coil loss, respectively. Since the losses of the inverter and the SAR change with the variation of the modulation depth, the optimum load resistance of IPT converter is indirectly affected. Therefore, for the design consideration of the control reference value  $R_{eq,opt}$ , a theoretical loss analysis can be applied to realize this issue.

For the inverter, the power loss  $P_{loss,inv}$  is consisted of the switching loss  $P_{sw,inv}$  and the conduction loss  $P_{con,inv}$  [44],



given by

$$P_{loss,inv} = P_{sw,inv} + P_{con,inv} \quad (18)$$

Supposed that switching loss calculation based on the linear approximation of drain-to-source voltage and current [45], [46],  $P_{sw,inv}$  can be estimated as

$$P_{sw,inv} = [i_{P,avg} v_{P,avg}(t_{on} + t_{off}) + C_{OSS,1} v_{P,avg}^2] f_{SW} \quad (19)$$

where  $t_{on}$  and  $t_{off}$  are turn-on time and turn-off time of the MOSFET switches, respectively, and  $C_{OSS,1}$  is output capacitance of each MOSFET switch in the inverter.  $v_{P,avg} = \frac{\pi|V_P|}{4}$  and  $i_{P,avg} = \frac{2|I_P|}{\pi}$  are the average value of  $v_P$  and  $i_P$  passing through the inverter, respectively.  $f_{SW}$  represents the operating frequency of IPT converter. Moreover, the conduction loss  $P_{cov,inv}$  can be estimated as

$$P_{con,inv} = 2[i_{P,rms}^2 R_{on,1} + i_{P,avg} V_{f,1}] \quad (20)$$

where  $R_{on,1}$  is the on-resistance of the MOSFET switches  $S_1$ - $S_4$ , and  $V_{f,1}$  is the forward voltage of their anti-parallel diodes.  $i_{P,rms} = \frac{|I_P|}{\sqrt{2}}$  is the rms value of  $i_P$ . Hence, incorporating the losses of the inverter in the transmitter side, equivalent series resistance  $R_P$  can be calculated as

$$R_P = R_{P,w} + \frac{P_{loss,inv}}{i_{P,rms}^2} \quad (21)$$

Similarly, considering the switching loss and the conduction loss of the SAR,  $P_{sw,SAR}$  and  $P_{con,SAR}$ , the power loss of the SAR  $P_{loss,SAR}$  is given by

$$P_{loss,SAR} = P_{sw,SAR} + P_{con,SAR} \quad (22)$$

Based on the linear approximation,  $P_{sw,SAR}$  can be eliminated as

$$P_{sw,SAR} = \frac{1}{2}[i_{S,avg} v_{S,avg}(t_{on} + t_{off}) + C_{OSS,2} v_{S,avg}^2] f_{SW} \quad (23)$$

where  $v_{S,avg} = \frac{\pi|V_S|}{4}$  and  $i_{S,avg} = \frac{2|I_S|}{\pi}$  are the average value of  $v_S$  and  $i_S$  injecting into the SAR, respectively. Then, the conduction loss in the SAR can be estimated as

$$P_{con,SAR} = i_{S,rms}^2 R_{on,2} + i_{S,avg} V_{f,2} \quad (24)$$

Assumed that the MOSFET switches  $S_7$  and  $S_8$  of the SAR is same as  $S_1$ - $S_4$ ,  $R_{on,2}$  is the on-resistance of the MOSFET switches  $S_7$ - $S_8$ . Likewise, the forward voltage of anti-parallel diode of the SAR  $V_{f,2}$  is equal to  $V_{f,1}$ .  $i_{S,rms} = \frac{|I_S|}{\sqrt{2}}$  is the rms value of  $i_S$ .  $C_{OSS,2}$  is output capacitance of each MOSFET switch in the SAR. Therefore, equivalent series resistance  $R_S$  can be calculated as

$$R_S = R_{S,w} + \frac{P_{loss,SAR}}{i_{S,rms}^2} \quad (25)$$

Based on above theoretical loss analysis, even though the loss resistance ratio  $\sqrt{\frac{R_P}{R_S}}$  has little deviation caused by the variation of the modulation depth of the SAR, we can still maintain the efficiency at the optimum value even under

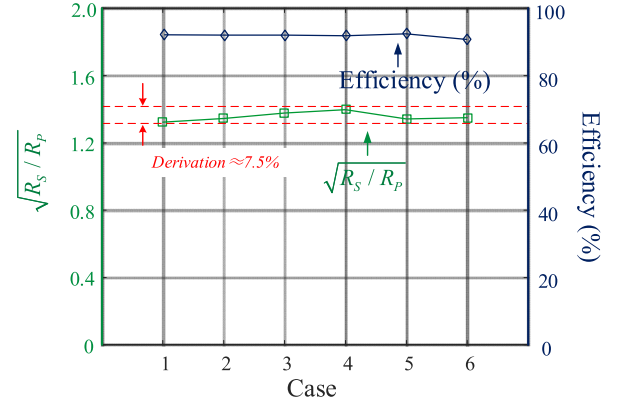


FIGURE 11. Loss resistance ratio  $\sqrt{\frac{R_P}{R_S}}$  and the transfer efficiency versus different irradiance cases.

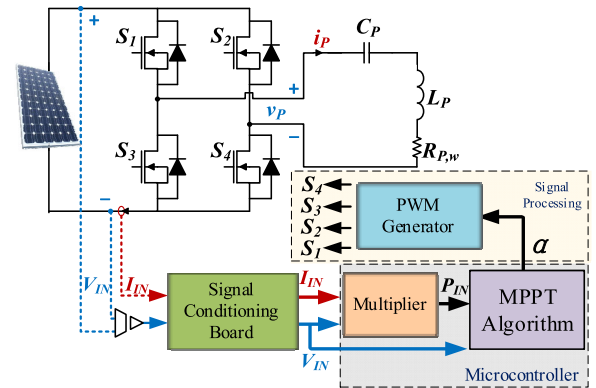


FIGURE 12. MPPT control scheme of the proposed PV-IWPT system.

various irradiance conditions (Case 1-6), as highlighted in the green curve of Fig. 11. However, it can be observed that, the efficiency will not be significantly affected and is maintained at the optimum value even if the irradiance is varied, as shown by the dark blue curve of Fig. 11. Therefore, in order to simplify the MEPT control in this paper, we fix the control reference as  $R_{eq,opt}$ .

## B. MPPT CONTROL SCHEME

In this PV-IWPT system, we implement the MPPT of the PV array by controlling the inverter instead of adding an extra DC-DC converter. From (17), by controlling the conduction angle  $\alpha$  of the inverter, we can vary the DC input resistance of the PV-IWPT converter, thus determining the output power of the PV array as mentioned in Section III-B. Fig. 12 shows the MPPT control scheme at the receiver-side of the PV-IWPT system. A signal conditional board senses the input voltage  $V_{IN}$  and the input current  $I_{IN}$  through a signal conditional board. Then, we calculate the input power  $P_{IN}$  with the help of a multiplier. With the sensed  $V_{IN}$  and the calculated  $P_{IN}$ , the MPPT algorithm computes the conduction angle  $\alpha$  of the inverter, in which we can adjust it accordingly to reach the maximum input power point of the PV array.

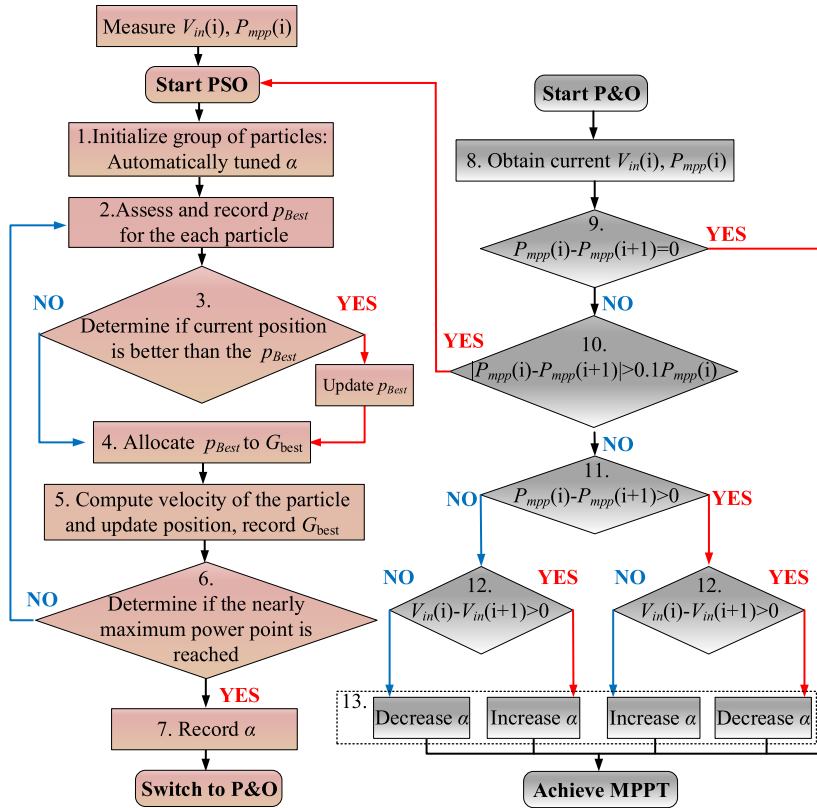


FIGURE 13. Flowchart of PSO with auxiliary P&O algorithm.

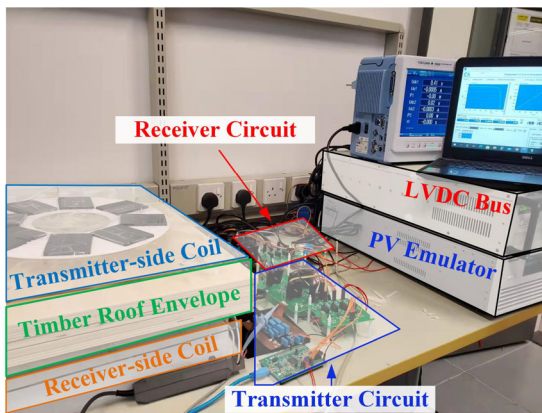


FIGURE 14. Experimental platform of the overall timbers-rooftop PV-IWPT system.

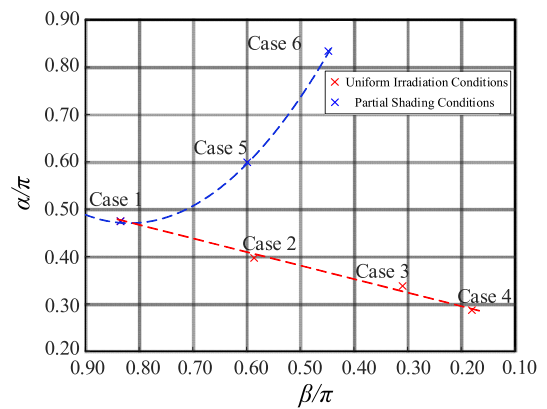


FIGURE 15. Measured operating points of the conduction angle  $\alpha$  and  $\beta$  under different irradiance cases (Case 1-6).

In this paper, we apply a hybrid MPPT control algorithm, PSO with auxiliary P&O, to ensure the effectiveness of the proposed PV-IWPT system even under various irradiance conditions (non-shading condition, uniform shading condition and partial shading condition). This hybrid control method has an advantage of the fast global maximum power point (GMPP) tracking ability of the PSO from the transition of uniform to partial shading conditions. Fig. 13 illustrates the flowchart of the proposed hybrid control strategy. For the left

part of the flowchart, we apply a conventional PSO algorithm to track the GMPP with a population of individual particles that keep tracking the neighboring particles, where  $p_{Best}$  is the local best position of a particle in a searching area,  $G_{Best}$  is the global best position of the whole population (MPP of the PV array) and  $i$  is the particle size within  $[1, \infty]$ . Then, we can model the particle position  $x_i$  as:

$$x_i[t + 1] = x_i[t] + v_i[t + 1] \tag{26}$$

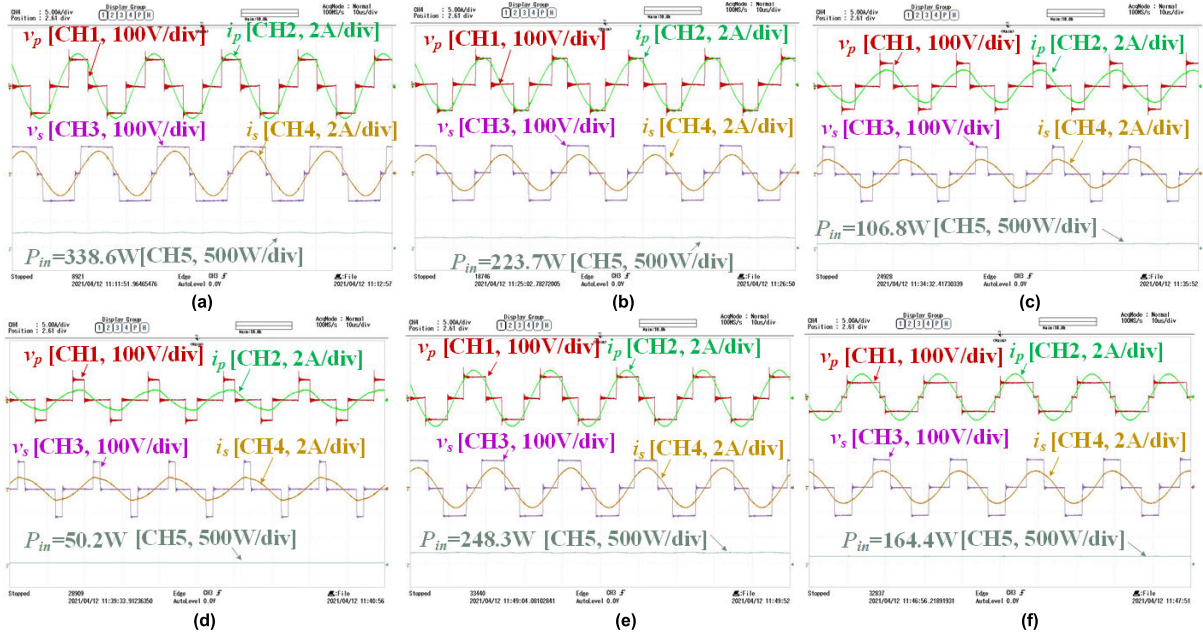


FIGURE 16. Measured operating waveforms of the inverter and the SAR under different irradiance cases (Case 1-6).

where  $t$  is the  $t$ -th iteration and  $v_i$  is the velocity of each particle. The fitness function of this system becomes:

$$p_i[t + 1] > p_i[t] \quad (27)$$

where the term  $p$  is the input power of the PV array.

First of all, we choose the conduction angle  $\alpha$  as the particle of this MPPT control, so it initializes a population of particles, automatically tuning  $\alpha$  (Step 1). The position of each particle corresponds to the output power of the PV panels, with the individual position  $x_i$  of each particle assessed and recorded. Among these individual positions, we can evaluate the local best positions in various areas (Step 2). For the comparison of the current position with the local best position  $p_{Best}$ , we can update  $G_{Best}$  for the next iteration if the best new position candidate exists (Step 3-Step 4), then we keep the computation of the velocity of particles and update their positions (Step 5). We further check the stop criterion of the PSO regarding the predefined convergence criteria. Otherwise, this searching strategy (Step 2-Step 5) will continue repeating itself. After approximately reaching GMPP, the PSO algorithm switches to a traditional P&O algorithm. The fine tracking employs the P&O algorithm (Step 8-Step 13), which has high tracking capability, low complexity, easy implementation and performs fast dynamic nature [47], as Fig. 13 shows (in the right part). This auxiliary P&O algorithm aims to help the PSO algorithm to handle small oscillations in solar irradiance or small variations of uniform shading conditions after reaching the GMPP, which reduces the power oscillations caused by the PSO due to the small variation cases.

## V. EXPERIMENTAL VERIFICATION

### A. SPECIFICATIONS AND EXPERIMENTAL PROTOTYPE

To verify the proposed PV-IWPT system along with the MEPT and MPPT control schemes, we built in the

TABLE 3. Experimental parameters.

| Symbol   | Parameter                | Value   |
|--|--------------------------|---|
| $L_p, L_s$   | Self-inductance          | 255.50 $\mu$ H, 370.40 $\mu$ H                                  |
| $k$  | Coupling coefficient     | 0.235   |
| $R_{p,w}, R_{s,w}$                                 | Coil resistance          | 0.25 $\Omega$ , 0.50 $\Omega$                                   |
| $f_{sw} = \omega/2\pi$                             | Operating frequency      | 50kHz   |
| $C_p, C_s$   | Compensation capacitance | 41.0nF, 28.5nF  |
| $C_{fs}$   | Output capacitance       | 1000 $\mu$ F  |
| $S_T-S_4$  | Inverter and SAR switch  | IPP60R099 with $V_{\approx}0.7V$ and $R_{on}\approx 0.01\Omega$ |
| $D_3, D_6$   | Diodes                   | MBR20200 with $V_{\approx}0.7V$                                 |
| $V_{IN}$   | Input voltage            | 0 - 129.8V  |
| $V_O$  | Output voltage           | 110V  |
| Transmitter-side (Tx) and Receiver-side (Rx) Coils |                          |   |
| $r_{out,Tx}, r_{out,Rx}$                           | Outer radius             | 16cm, 16cm  |
| $r_{in,Tx}, r_{in,Rx}$                             | Inner radius             | 8cm, 6cm  |
| $N_{Tx}, N_{Rx}$                                   | Number of turns          | 26turns, 32 turns   |

laboratory a scale-down 500W experimental prototype (Fig. 14) with the system parameters given in Table 3. In the experiment, we emulate the PV array with a programmable DC power supply Chroma 62050H-600S, that emulates the non-shading condition (Case 1), uniform shading conditions (Case 2-Case 4) and partial shading conditions (Case 5-Case 6). Roof timbers with thickness of 14cm separates both the transmitter and the receiver coils with circular spiral windings. An electronic load working on the constant voltage mode emulates the LVDC bus.

### B. MEASURED WAVEFORMS AND OPERATING POINTS

Fixing the operating frequency at 50kHz, we adjust the conduction angle  $\alpha$  of the inverter to track the maximum power

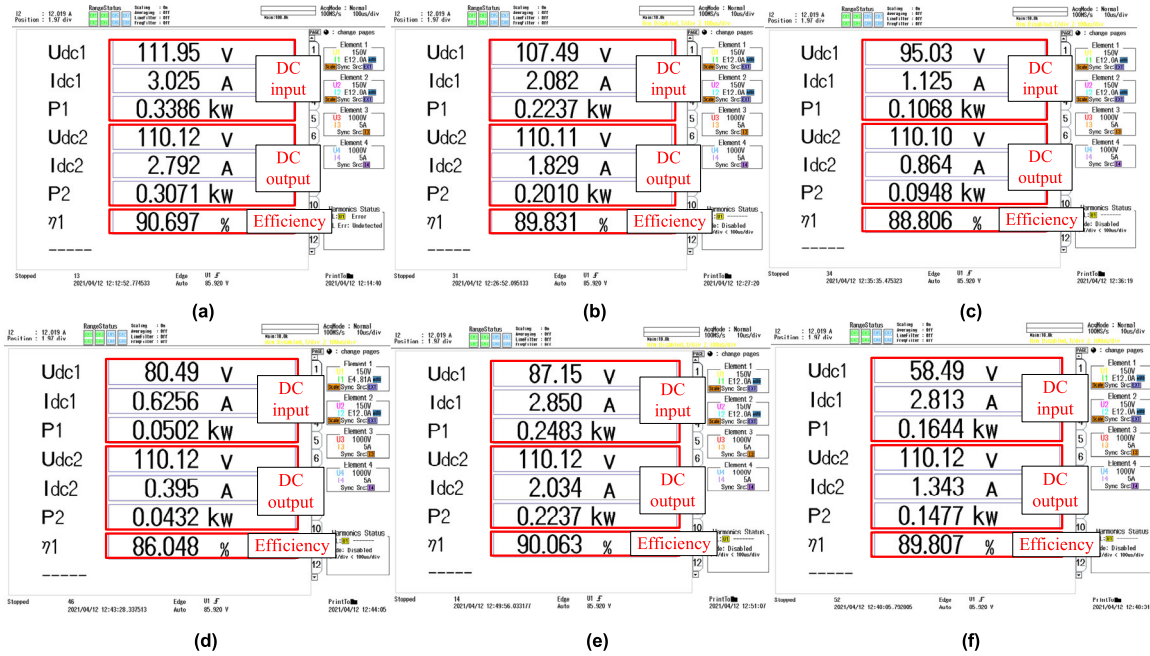


FIGURE 17. Screen capture of experimental input power, output power and DC-to-DC efficiency under different shading cases (Case 1-6).

point. Meanwhile, we adjust the conduction angle  $\beta$  of the SAR to track the maximum efficiency point. Fig. 15 shows the measured operating points under the uniform irradiation conditions and partial shading conditions. From the red curve of Fig. 15, the conduction angle  $\alpha$  decreases from  $0.475\pi$  to  $0.287\pi$  and the conduction angle  $\beta$  decreases from  $0.834\pi$  to  $0.180\pi$  since the corresponding maximum DC input resistance  $R_{IN,MAX}$  and the maximum input power  $P_{MAX}$  of the PV array decreases, respectively, which is caused by the variations from the non-shading condition to the uniform shading conditions (Case 1 to Case 4). On the other hand, from the blue curve of Fig. 15, the conduction angle  $\alpha$  increases from  $0.475\pi$  to  $0.834\pi$  and the conduction angle  $\beta$  decreases from  $0.834\pi$  to  $0.440\pi$ , which represents the variations from the non-shading condition to the partial shading cases (Case 5 and Case 6). This happens because  $R_{IN,MAX}$  of Case 1, Case 5 and Case 6 increases in succession caused by the partial shading. This result is consistent with the analysis in Section III. In addition, Fig. 16 shows the waveforms of the inverter, the SAR, and the corresponding output power in 6 different shading cases. Moreover, the screen captures of the experimental input power, output power and DC-to-DC efficiency by using Yokogawa PX8000 Precision Power Scope are given in Fig. 17.

C. COMPARISON OF PV-IWPT SYSTEM EFFICIENCY

As mentioned in Section I, the conventional PV-IWPT systems [20], [21], [22], [23], [24], [29] lack the maximum efficiency tracking control, resulting in poor transfer efficiency during the irradiance variation conditions. For the experimental platform (Gap: Timbers with thickness of 14cm,

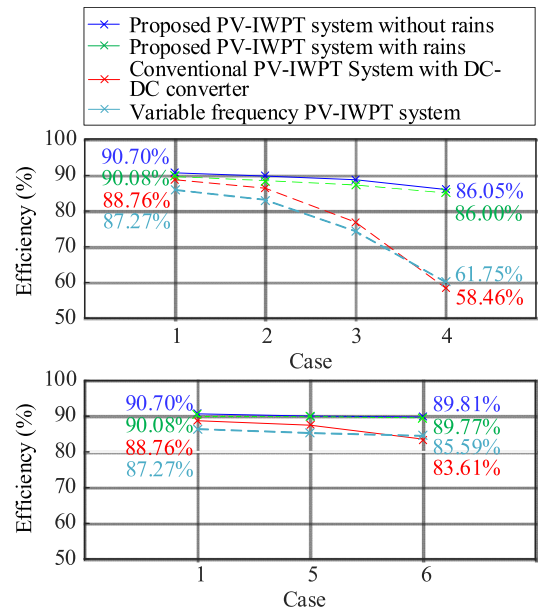


FIGURE 18. Measured PV-IWPT system efficiency of the conventional PV-IPT system with DC-DC converter, variable frequency PV-IPT system, and the proposed PV-IWPT system with or without rains under various shading conditions.

$k = 0.235$ ) under various shading conditions including Case 1 to Case 6, the corresponding measured efficiency of the PV-IWPT system with DC-DC converter [20], [21], [22], [23], [24], variable frequency PV-IWPT system [29] and the proposed PV-IWPT system are plotted in Fig. 18, which clearly indicates that the DC-to-DC efficiency of the

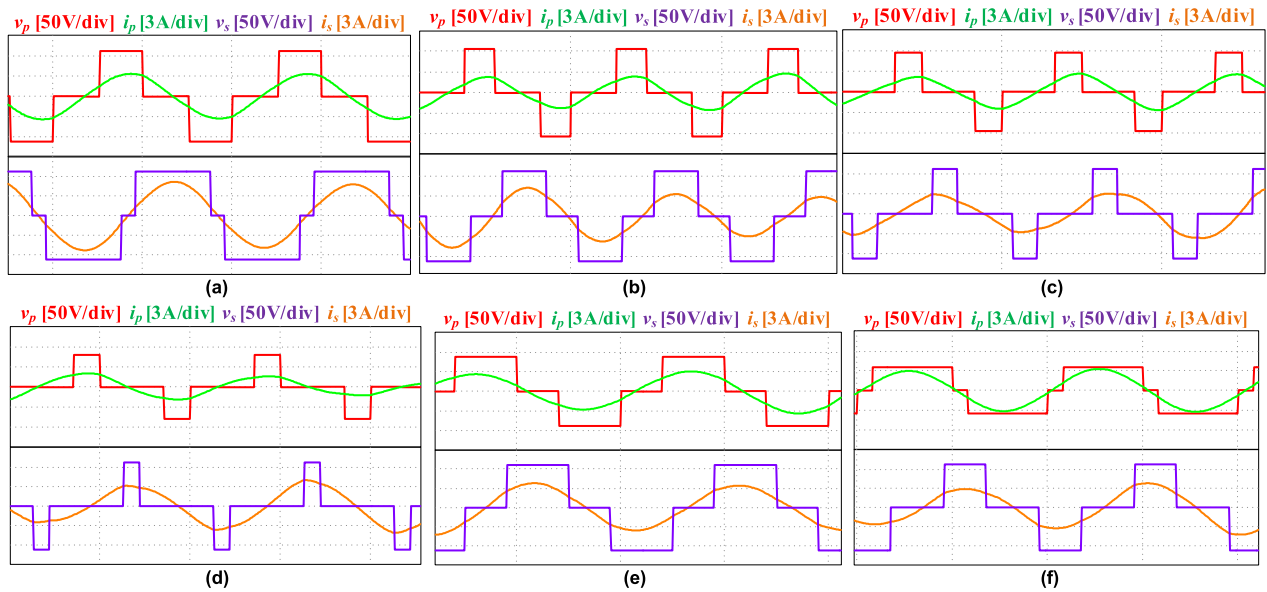


FIGURE 19. Simulated operating waveforms of the inverter and the SAR under different irradiance cases (Case 1-6).

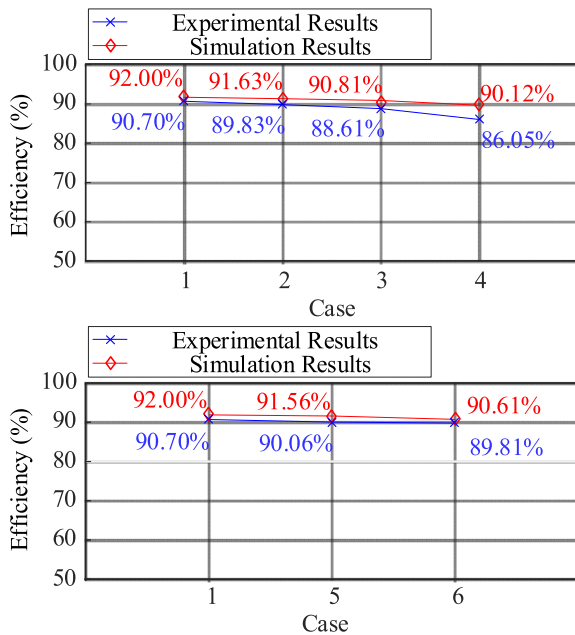


FIGURE 20. Comparison between experimental and simulated efficiency of the proposed PV-IWPT system under various shading conditions.

proposed PV-IWPT system with MEPT can keep a value over 86%, which is highest among the PV-IWPT systems under the 6 different irradiance cases. In particular, under uniform shading conditions, the efficiency difference between the proposed system and the PV-IWPT system with DC-DC converter is more than 27% in Case 4. When there is variation of the irradiance, it significantly influences the equivalent load, thus causing high degradation of the system efficiency. From Fig. 18, the proposed system takes the advantage of the MEPT control to maintain a high transfer efficiency

even under different irradiance conditions, which is the main contribution of this system. In addition, aiming to do a comprehensive analysis of the proposed PV-IWPT system, we also simulate the system by using Software PSIM. The operating waveforms of the inverter and the SAR under different irradiance cases (Case 1-6) are shown in Fig. 19. Then, the corresponding comparison between the experimental and simulated efficiency of the proposed PV-IWPT system under various shading conditions are given in Fig. 20. In more details, the experimental efficiency is closed with the simulated efficiency and the trend of the experimental results is also consistent with the simulation results, which verify the validity of the proposed PV-IWPT system.

#### D. CONSIDERATION OF THE RAINY ISSUE

Since the rooftop PV panels are implemented outside the roof as shown in Fig. 2 (c), the raindrops may penetrate the construction products [18] between the transmitter-side coil and the exterior roof during raining. In this situation, the magnetic medium is not only the roof timber, but also some raindrops. Aiming to verify the practicality of the proposed PV-IWPT system under the rainy issue, we provided an extreme experiment in which the magnetic mediums are timber and water as shown in Fig. 21, the efficiency comparison of the proposed PV-IWPT system with rains and without rains under various shading conditions are also shown in Fig. 18, which clearly verify that proposed PV-IWPT system can maintain the system performance of the proposed PV-IWPT system even under rainy issue.

#### E. TRANSIENT RESPONSE FOR VARIATIONS OF IRRADIATION

A closed-loop controller, implemented with a STM32F4 microcontroller, aims to verify the transient response

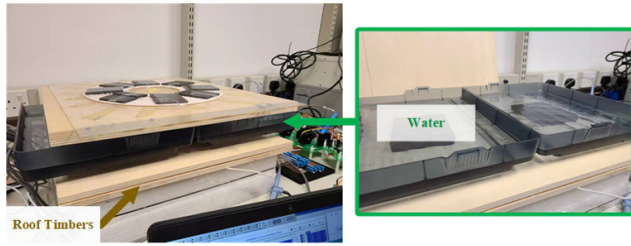


FIGURE 21. An extreme experiment where the magnetic mediums are timber and water.

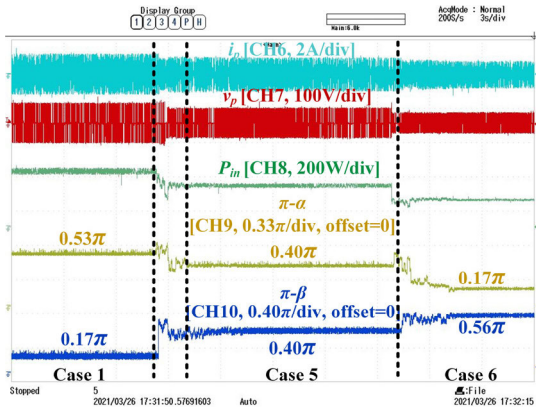


FIGURE 22. Transient waveforms ( $i_p$ ,  $v_p$ ,  $\pi-\alpha$ ,  $\pi-\beta$ ) varying from Case 1 to Case 5 and then to Case 6.

capability and feasibility of the proposed PV-IWPT system under variations of the irradiation. Fig. 22 shows that the transient waveforms vary from a non-shading condition (Case 1) to partial shading conditions (Case 5 and Case 6). The ac input current  $i_p$  and voltage  $v_p$  are CH6 in cyan and CH7 in red, respectively. We calculate the input power represented as CH8 in green, by using  $I_O$  and  $V_O$ . To observe the control variables, we use the digital-to-analog output, where CH9 represents the phase shift angle  $\pi-\alpha$  of the inverter in yellow and CH10 represents the phase shift angle  $\pi-\beta$  of the SAR. Also, no wireless communication is necessary for the control of the proposed PV-IWPT system.

## VI. CONCLUSION

This paper proposed a novel rooftop PV-IWPT system, which can simultaneously track 1) the maximum input power extracted from the PV array through the direct MPPT control of the inverter, and 2) the maximum transfer efficiency of the SS-IWPT converter through the direct MEPT control of the SAR. In this work, we developed a hybrid PSO based P&O MPPT algorithm in the direct MPPT control of the transmitter side by controlling the conduction angle  $\alpha$  of the inverter. Aiming to alleviate the transfer efficiency degradation effects caused by the variations of shading conditions and even rainy condition, we applied a simple load impedance matching in the direct MEPT control of the receiver side, by controlling the conduction angle  $\beta$  of the SAR. Moreover, we fixed

the system operating frequency, and the wireless feedback communication is not necessary for the control operations of both transmitter and receiver sides, which simplifies the overall PV-IWPT system.

## REFERENCES

- [1] K. Jia, Z. Yang, Y. Fang, T. Bi, and M. Sumner, "Influence of inverter-interfaced renewable energy generators on directional relay and an improved scheme," *IEEE Trans. Power Electron.*, vol. 34, no. 12, pp. 11843–11855, Dec. 2019.
- [2] W. Dong, Z. Lu, L. He, L. Geng, X. Guo, and J. Zhang, "Low-carbon optimal planning of an integrated energy station considering combined power-to-gas and gas-fired units equipped with carbon capture systems," *Int. J. Electr. Power Energy Syst.*, vol. 138, Jun. 2022, Art. no. 107966.
- [3] C.-Y. Yang, C.-Y. Hsieh, F.-K. Feng, and K.-H. Chen, "Highly efficient analog maximum power point tracking (AMPPT) in a photovoltaic system," *IEEE Trans. Circuits Syst. I, Reg. Papers*, vol. 59, no. 7, pp. 1546–1556, Jul. 2012.
- [4] M. S. Keerthana, G. Uma, and U. Sowmmiya, "A study of a solar PV and wind-based residential DC NanoGrid with dual energy storage system under islanded/interconnected/grid-tied modes," *Int. J. Electr. Power Energy Syst.*, vol. 143, Dec. 2022, Art. no. 108473.
- [5] D. Dong, I. Cvetkovic, D. Boroyevich, W. Zhang, R. Wang, and P. Mattavelli, "Grid-interface bidirectional converter for residential DC distribution systems—Part one: High-density two-stage topology," *IEEE Trans. Power Electron.*, vol. 28, no. 4, pp. 1655–1666, Apr. 2013.
- [6] S. Peyghami, H. Mokhtari, and F. Blaabjerg, "Autonomous power management in LVDC microgrids based on a superimposed frequency droop," *IEEE Trans. Power Electron.*, vol. 33, no. 6, pp. 5341–5350, Jun. 2018.
- [7] P. Mohammadi and S. Mehraeen, "Challenges of PV integration in low-voltage secondary networks," *IEEE Trans. Power Del.*, vol. 32, no. 1, pp. 525–535, Feb. 2017.
- [8] S. Peyghami, P. Davari, H. Mokhtari, and F. Blaabjerg, "Decentralized droop control in DC microgrids based on a frequency injection approach," *IEEE Trans. Smart Grid*, vol. 10, no. 6, pp. 6782–6791, Nov. 2019.
- [9] M. Nasir, Z. Jin, H. A. Khan, N. A. Zaffar, J. C. Vasquez, and J. M. Guerrero, "A decentralized control architecture applied to DC nanogrid clusters for rural electrification in developing regions," *IEEE Trans. Power Electron.*, vol. 34, no. 2, pp. 1773–1785, Feb. 2019.
- [10] B. Liu, S. Duan, and T. Cai, "Photovoltaic DC-building-module-based BIPV system—Concept and design considerations," *IEEE Trans. Power Electron.*, vol. 26, no. 5, pp. 1418–1429, May 2011.
- [11] M. Sechilariu, B. Wang, and F. Locment, "Building integrated photovoltaic system with energy storage and smart grid communication," *IEEE Trans. Ind. Electron.*, vol. 60, no. 4, pp. 1607–1618, Apr. 2013.
- [12] M. Rentschler and I. Bhattacharya, "Decoupled control of wireless power transfer: Eliminating the interdependence of load resistance and coupling to achieve a simple control framework with fast response times," *Int. J. Electr. Power Energy Syst.*, vol. 99, pp. 1–10, Jul. 2018.
- [13] A. Kuperman, "Additional two-capacitor basic compensation topologies for resonant inductive WPT links," *IEEE Trans. Power Del.*, vol. 35, no. 5, pp. 2568–2570, Oct. 2020.
- [14] T. Tan, K. Chen, Q. Lin, Y. Jiang, L. Yuan, and Z. Zhao, "Impedance shaping control strategy for wireless power transfer system based on dynamic small-signal analysis," *IEEE Trans. Circuits Syst. I, Reg. Papers*, vol. 68, no. 3, pp. 1354–1365, Mar. 2021.
- [15] E. Holton, A. Halbe, A. Garney, J. Whitbeck, K. Sharpe, D. Metacarpa, and P. Haldar, "Cost and market analysis of integrative lightweight PV systems for low-slope commercial rooftops," in *Proc. IEEE 40th Photovolt. Spec. Conf. (PVSC)*, Jun. 2014, pp. 2740–2742.
- [16] R. J. Yang, "Overcoming technical barriers and risks in the application of building integrated photovoltaics (BIPV): Hardware and software strategies," *Autom. Construct.*, vol. 51, pp. 92–102, Mar. 2015.
- [17] B. Minnaert, S. Ravyts, J. Driesen, and N. Stevens, "Challenges for wireless power transfer in building-integrated photovoltaics," in *Proc. IEEE PELS Workshop Emerg. Technol., Wireless Power Transf.*, Jun. 2018, pp. 1–5.
- [18] H. Gholami, H. Nils Røstvik, and K. Steemers, "The contribution of building-integrated photovoltaics (BIPV) to the concept of nearly zero-energy cities in Europe: Potential and challenges ahead," *Energies*, vol. 14, no. 19, p. 6015, Sep. 2021.

- [19] A. Stepanov, "Galvanically isolated MPPT DC/DC converter for PV system tied to DC grid," in *Proc. IEEE 3rd Workshop Adv. Inf., Electron. Electr. Eng. (AIEEE)*, Nov. 2015, pp. 1–4.
- [20] A. Ghosh, A. Ukil, and A. P. Hu, "PV-battery system with wireless power transfer for LV applications," in *Proc. 46th Annu. Conf. IEEE Ind. Electron. Soc.*, Oct. 2020, pp. 4283–4287.
- [21] A. Ghosh, A. Ukil, and A. P. Hu, "Integration of rooftop solar PV generation with wireless power transfer," in *Proc. IEEE PES Asia-Pacific Power Energy Eng. Conf. (APPEEC)*, Dec. 2019, pp. 1–5.
- [22] Y. Zheng, Z. Cheng, C. Liu, H. Liu, M. Amirabadi, and B. Lehman, "Modular wireless power transmission for photovoltaic subpanel system," in *Proc. IEEE Energy Convers. Congr. Expo. (ECCE)*, Vancouver, BC, Canada, Oct. 2021, pp. 546–553.
- [23] M. Elwalaty, M. Jemli, and H. B. Azza, "A two-rectangular coils wireless charging electric vehicle with photovoltaic generator," in *Proc. 19th Int. Conf. Sci. Techn. Autom. Control Comput. Eng. (STA)*, Sousse, Tunisia, Mar. 2019, pp. 455–460.
- [24] A. Shahin, J.-P. Martin, S. Pierfederici, and A. M. Sharaf, "Integration of renewable energy sources to wireless charger of electrical vehicle," in *Proc. 22nd IEEE Int. Conf. Ind. Technol. (ICIT)*, Valencia, Spain, vol. 1, Mar. 2021, pp. 397–402.
- [25] E. Koutroulis, N. Sason, and V. Georgiadis, "Combined tracking of the maximum power and maximum efficiency operating points for real-time maximization of the energy production of PV systems," *IEEE Trans. Power Electron.*, vol. 34, no. 9, pp. 8634–8645, Sep. 2019.
- [26] S. Bhattacharyya, D. S. Kumar P, S. Samanta, and S. Mishra, "Steady output and fast tracking MPPT (SOFT-MPPT) for P&O and InC algorithms," *IEEE Trans. Sustain. Energy*, vol. 12, no. 1, pp. 293–302, Jan. 2021.
- [27] H. Li, D. Yang, W. Su, J. Lü, and X. Yu, "An overall distribution particle swarm optimization MPPT algorithm for photovoltaic system under partial shading," *IEEE Trans. Ind. Electron.*, vol. 66, no. 1, pp. 265–275, Jan. 2019.
- [28] J. Jose and J. P. Therattil, "WPT compensation topology optimized for PV embedded electric vehicle," *Sustain. Energy Technol. Assessments*, vol. 53, Oct. 2022, Art. no. 102605.
- [29] D. Baros, D. Voglitsis, N. P. Papanikolaou, A. Kyritsis, and N. Rigogiannis, "Wireless power transfer for distributed energy sources exploitation in DC microgrids," *IEEE Trans. Sustain. Energy*, vol. 10, no. 4, pp. 2039–2049, Oct. 2019.
- [30] W. Zhong and S. Y. Hui, "Reconfigurable wireless power transfer systems with high energy efficiency over wide load range," *IEEE Trans. Power Electron.*, vol. 33, no. 7, pp. 6379–6390, Jul. 2018.
- [31] Z. Huang, C. Lam, P. Mak, R. P. d. S. Martins, S. Wong, and C. K. Tse, "A single-stage inductive-power-transfer converter for constant-power and maximum-efficiency battery charging," *IEEE Trans. Power Electron.*, vol. 35, no. 9, pp. 8973–8984, Sep. 2020.
- [32] Z. Huang, S. Wong, and C. K. Tse, "Control design for optimizing efficiency in inductive power transfer systems," *IEEE Trans. Power Electron.*, vol. 33, no. 5, pp. 4523–4534, May 2018.
- [33] W. X. Zhong and S. Y. R. Hui, "Maximum energy efficiency tracking for wireless power transfer systems," *IEEE Trans. Power Electron.*, vol. 30, no. 7, pp. 4025–4034, Jul. 2015.
- [34] Z. Liao, Q. Feng, C. Jiang, F. Wu, C. Xia, and D. Yu, "Analysis and design of EIT-like magnetic coupling wireless power transfer systems," *IEEE Trans. Circuits Syst. I, Reg. Papers*, vol. 68, no. 7, pp. 3103–3113, Jul. 2021.
- [35] T. Nagashima, X. Wei, E. Bou, E. Alarcón, M. K. Kazimierczuk, and H. Sekiya, "Analysis and design of loosely inductive coupled wireless power transfer system based on class-E<sup>2</sup> DC–DC converter for efficiency enhancement," *IEEE Trans. Circuits Syst. I, Reg. Papers*, vol. 62, no. 11, pp. 2781–2791, Nov. 2015.
- [36] H. Zhu, D. Zhang, H. S. Athab, B. Wu, and Y. Gu, "PV isolated three-port converter and energy-balancing control method for PV-battery power supply applications," *IEEE Trans. Ind. Electron.*, vol. 62, no. 6, pp. 3595–3606, Jun. 2015.
- [37] O. D. Montoya, W. Gil-González, and A. Garces, "Numerical methods for power flow analysis in DC networks: State of the art, methods and challenges," *Int. J. Electr. Power Energy Syst.*, vol. 123, Dec. 2020, Art. no. 106299.
- [38] W. Zhang, S.-C. Wong, C. K. Tse, and Q. Chen, "Load-independent duality of current and voltage outputs of a series- or parallel-compensated inductive power transfer converter with optimized efficiency," *IEEE J. Emerg. Sel. Topics Power Electron.*, vol. 3, no. 1, pp. 137–146, Mar. 2015.
- [39] W. Zhang, S.-C. Wong, C. K. Tse, and Q. Chen, "Analysis and comparison of secondary series- and parallel-compensated inductive power transfer systems operating for optimal efficiency and load-independent voltage-transfer ratio," *IEEE Trans. Power Electron.*, vol. 29, no. 6, pp. 2979–2990, Jun. 2014.
- [40] C.-S. Wang, G. A. Covic, and O. H. Stielau, "Power transfer capability and bifurcation phenomena of loosely coupled inductive power transfer systems," *IEEE Trans. Ind. Electron.*, vol. 51, no. 1, pp. 148–157, Feb. 2004.
- [41] I. Iam, I. Hoi, Z. Huang, C. Gong, C. Lam, P. Mak, and R. P. D. S. Martins, "Constant-frequency and noncommunication-based inductive power transfer converter for battery charging," *IEEE J. Emerg. Sel. Topics Power Electron.*, vol. 10, no. 2, pp. 2147–2162, Apr. 2022.
- [42] Z. Huang, S. Wong, and C. K. Tse, "An inductive-power-transfer converter with high efficiency throughout battery-charging process," *IEEE Trans. Power Electron.*, vol. 34, no. 10, pp. 10245–10255, Oct. 2019.
- [43] A. Urtausan and D. D. Lu, "Control of a single-switch two-input buck converter for MPPT of two PV strings," *IEEE Trans. Ind. Electron.*, vol. 62, no. 11, pp. 7051–7060, Nov. 2015.
- [44] X. Li, X. Li, P. Liu, S. Guo, L. Zhang, A. Q. Huang, X. Deng, and B. Zhang, "Achieving zero switching loss in silicon carbide MOSFET," *IEEE Trans. Power Electron.*, vol. 34, no. 12, pp. 12193–12199, Dec. 2019.
- [45] R. Erickson and D. Maksimovic, *Fundamentals of Power Electronics*. Cham, Switzerland: Springer, 2001, pp. 92–100.
- [46] Z. Shen, Y. Xiong, X. Cheng, Y. Fu, and P. Kumar, "Power MOSFET switching loss analysis: A new insight," in *Proc. Conf. Rec. IEEE Ind. Appl. Conf. 41st IAS Annu. Meeting*, Oct. 2006, pp. 1438–1442.
- [47] R. B. Bollipo, S. Mikkili, and P. K. Bonthagorla, "Hybrid, optimal, intelligent and classical PV MPPT techniques: A review," *CSEE J. Power Energy Syst.*, vol. 7, no. 1, pp. 9–33, Jan. 2021.



**IO-WA IAM** (Student Member, IEEE) received the B.Sc. degree in electrical and computer engineering from the University of Macau (UM), Macao, China, in 2020, where he is currently pursuing the Ph.D. degree in electrical and computer engineering.

His current research interests include power electronics and wireless power transfer. He was awarded the Best Track Paper Award in APPEEC, in 2019.



**ZHAOYI DING** (Student Member, IEEE) received the B.Sc. degree in electrical engineering and automation from the Harbin Institute of Technology (HIT), Harbin, China, in 2018. He is currently pursuing the M.Sc. degree in electrical and computer engineering with the University of Macau (UM), Macao, China.

His current research interests include power electronics and wireless power transfer.



**ZHICONG HUANG** (Member, IEEE) received the B.Eng. degree in electrical engineering and automation and the M.Eng. degree in mechanical and electronic engineering from the Huazhong University of Science and Technology, Wuhan, China, in 2010 and 2013, respectively, and the Ph.D. degree in power electronics from The Hong Kong Polytechnic University, Hong Kong, in 2018.

He is currently an Associate Professor with the Shien-Ming Wu School of Intelligent Engineering, South China University of Technology, Guangzhou, China. From January 2019 to February 2020, he was a Postdoctoral Fellow with the UM Macao Talent Program, State Key Laboratory of Analog and Mixed-Signal VLSI, University of Macau, Macao, China. His research interests include wireless power transfer, power electronics penetrated power systems, electric vehicle, and intelligent engineering.

Dr. Huang received the Outstanding Reviewer Award from IEEE TRANSACTIONS ON POWER ELECTRONICS, in 2021.



**CHI-SENG LAM** (Senior Member, IEEE) received the Ph.D. degree in electrical and electronics engineering from the University of Macau (UM), Macao, China, in 2012.

In 2013, he was a Postdoctoral Fellow with The Hong Kong Polytechnic University, Hong Kong, China. He completed the Clare Hall Study Program with the University of Cambridge, Cambridge, U.K., in 2019. He is currently an Associate Professor with the State Key Laboratory of Analog and Mixed-Signal VLSI and the Institute of Microelectronics, UM, and the Department of Electrical and Computer Engineering, Faculty of Science and Technology, UM. He has coauthored or co-edited four books and more than 160 technical journals and conference papers. He holds six U.S. and five Chinese patents. His research interests include power quality compensators, renewable energy generation, power management integrated circuits, and wireless power transfer.

Dr. Lam was a recipient or co-recipient of the IEEE PES Chapter Outstanding Engineer Award, in 2016, and the Macao Science and Technology Invention Award (Third Class and Second Class), in 2014 and 2018. He was awarded the 2021 IEEE ACCESS Outstanding Associate Editor. He is currently the Chair of the IEEE Macau IES Chapter and the Secretary of the IEEE IES Technical Committee on Power Electronics. He currently serves as an Associate Editor for the IEEE TRANSACTIONS ON INDUSTRIAL ELECTRONICS, the IEEE OPEN JOURNAL OF THE INDUSTRIAL ELECTRONICS SOCIETY, and IEEE ACCESS.



**RUI P. MARTINS** (Fellow, IEEE) received the Ph.D. degree in electrical engineering and computers from the Department of Electrical and Computer Engineering, Instituto Superior Técnico, University of Lisbon, Portugal, in 1992.

He has been with the Department of Electrical and Computer Engineering, Instituto Superior Técnico, University of Lisbon, since October 1980. Since 1992, he has been on leave from the University of Lisbon and the Department of Electrical and Computer Engineering, Faculty of Science and Technology, University of Macau, Macao, China, where he has been a Chair Professor, since August 2013. He was the Founding Director of the State Key Laboratory of Analog and Mixed-Signal VLSI, University of Macau, from 2011 to 2022. Since July 2010, he has been an Academician with the Lisbon Academy of Sciences, Portugal. He is currently the Director of the Institute of Microelectronics, University of Macau. He has authored or coauthored more than 900 publications, including ten books, 12 book chapters, 50 patents, more than 300 articles in scientific journals, and more than 400 papers in conference proceedings. His research interest includes analog and mixed-signal VLSI designs. He received the Author Recognition Award at the 70 years of ISSCC, in 2023, as a Top Contributor with more than 50 articles, and three Medals from Macao Government, in 1999, 2001, and 2021.



**PUI-IN MAK** (Fellow, IEEE) received the Ph.D. degree from the University of Macau (UM), Macao, China, in 2006.

He is currently a Professor with the UM Faculty of Science and Technology–ECE, the Director of the UM State Key Laboratory of Analog and Mixed-Signal VLSI, and the Deputy Director (Research) of the UM Institute of Microelectronics. His research interests include analog and radio-frequency (RF) circuits and systems for wireless and multidisciplinary innovations. He is a fellow of the Institution of Engineering and Technology (IET) and the U.K. Royal Society of Chemistry (RSC). He is/was the TPC Member of A-SSCC, from 2013 to 2016, ESS-CIRC, from 2016 to 2017, and ISSCC, from 2017 to 2019. He received the Xplorer Prize from the Tencent Foundation, in 2022. He was a Distinguished Lecturer of the IEEE Circuits and Systems Society, from 2014 to 2015, and the IEEE Solid-State Circuits Society, from 2017 to 2018. He has been inducted as an Overseas Expert of the Chinese Academy of Sciences since 2018. He is currently an Associate Editor of IEEE SOLID-STATE CIRCUITS LETTERS, in 2017, and IEEE JOURNAL OF SOLID-STATE CIRCUITS, in 2018.

• • •